remote sensing

MDPI

Article

Spectral Unmixing of Airborne and Ground-Based Imaging Spectroscopy for Pigment-Specific FAPAR and Sun-Induced Fluorescence Interpretation

Ana B. Pascual-Venteo [1,*], Adrián Pérez-Suay [1], Miguel Morata [1], Adrián Moncholí [1], Maria Pilar Cendrero-Mateo [1], Jorge Vicent Servera [1], Bastian Siegmann [2] and Shari Van Wittenberghe [1]

[1] Image Processing Laboratory, Universitat de València, 46010 València, Spain; adrian.perez@uv.es (A.P.-S.); miguel.morata@uv.es (M.M.); adrian.moncholi@uv.es (A.M.); m.pilar.cendrero@uv.es (M.P.C.-M.); jorge.vicent@uv.es (J.V.S.); shari.wittenberghe@uv.es (S.V.W.)

[2] Institute of Bio- and Geosciences Plant Sciences, Forschungszentrum Jülich GmbH, 52428 Jülich, Germany; b.siegmann@fz-juelich.de

* Correspondence: ana.b.pascual@uv.es

Highlights

What are the main findings?

- Constrained Least Squares (CLS) spectral unmixing provides robust and physically plausible estimates of pigment-specific absorbance from hyperspectral data.
- Airborne (HyPlant) and ground-based (FloX) observations show strong agreement in retrieved $fAPAR_{Chl\ a}$ and fluorescence quantum efficiency (FQE).

What are the implication of the main findings?

- The proposed framework enables consistent estimation of photosynthetic efficiency across sensing scales using combined reflectance and SIF information.
- Results establish a reliable baseline for monitoring photosynthetic performance in healthy crops and support future stress detection studies.

Abstract

Accurate quantification of photosynthetically active radiation absorbed by chlorophyll ($fAPAR_{Chl\ a}$) and the corresponding fluorescence quantum efficiency (FQE) is critical for understanding vegetation productivity. In this study, we investigate the retrieval of pigment-specific effective absorbance and Sun-Induced Chlorophyll Fluorescence (SIF) using both airborne hyperspectral imagery (HyPlant) and ground-based field spectroscopy (FloX) over a well-irrigated alfalfa field in northeastern Spain. Spectral unmixing techniques, including Constrained Least Squares (CLS), Potential Function (POT), and Bilinear (BIL) models, were applied to disentangle pigment and background contributions. The CLS approach was identified as the most robust, balancing reconstruction accuracy with physical plausibility. We derived $fAPAR_{Chl\ a}$ from the abundance-weighted pigment absorbance and combined it with spectrally-integrated SIF to calculate FQE. Comparisons between airborne and ground-based measurements revealed strong agreement, highlighting the potential of this combined methodology. The study demonstrates the applicability of advanced spectral unmixing frameworks for both airborne and proximal sensing data, providing a reliable baseline for photosynthetic efficiency in a healthy crop and establishing a foundation for future stress detection studies.

Keywords: Sun-Induced Chlorophyll Fluorescence (SIF); spectral unmixing; HyPlant; hyperspectral; spectral abundance; CAL/VAL

Academic Editor: Salah Bourennane

Received: 5 December 2025
Revised: 22 December 2025
Accepted: 29 December 2025
Published: 1 January 2026

1. Introduction

Photosynthesis is a critical process in the Earth's ecosystem, sustaining global biomass and biofuel production. Consequently, it has become a central focus of research in the Earth and life sciences [1,2]. Since the 1970s, remote sensing techniques have been employed to study plant photosynthesis in vivo, enabling deeper insights into plant behaviour within a dynamic global context. These studies often rely on light use efficiency models, first introduced by Monteith [3]. A key input for such models has traditionally been the estimation of vegetation greenness, which serves as a proxy for chlorophyll (Chl) content and potential photosynthetic capacity.

However, the growing impact of climate change is significantly altering the photosynthetic performance of global vegetation, threatening food production, and disrupting the balance between carbon sinks and sources [4]. This has intensified the need for global strategies aimed at early stress detection and continuous monitoring of photosynthesis. Such approaches are increasingly prioritised within current and emerging remote sensing frameworks [5–7].

Recent and upcoming hyperspectral and imaging spectroscopy missions, such as EnMAP [8] (Environmental Mapping and Analysis Program), PRISMA [9] (Hyperspectral Precursor of the Application Mission), and FLEX [6] (Fluorescence Explorer), offer unprecedented opportunities to enhance existing global vegetation products and to develop new ones. In particular, the European Space Agency's FLEX mission will deploy the Fluorescence Imaging System (FLORIS), an advanced imaging spectrometer specifically designed to explore methods for retrieving actual, or "true", photosynthesis.

The FLEX–FLORIS sensor has been designed to meet the dual objectives of detecting solar-induced chlorophyll fluorescence (SIF) and providing complementary products necessary for its interpretation [10]. This mission distinguishes itself from others focused on atmospheric or trace gas studies, which typically employ fluorescence as a linear proxy of vegetation carbon uptake, primarily driven by absorbed photosynthetically active radiation (PAR) [11]. Airborne imaging spectrometers targeting fluorescence, such as HyPlant [12,13], FIREFLY [14], NASA's Chlorophyll Fluorescence Imaging Spectrometer [15] (CFIS), and the Chlorophyll-Fluorescence Imager (Headwall Hyperspec, Bolton, MA, USA), are currently deployed on aircraft. These systems are often combined with hyperspectral sensors capable of meeting the requirements for assessing actual photosynthesis.

The HyPlant sensor is an advanced airborne hyperspectral imaging system designed for high-resolution remote sensing applications, particularly vegetation monitoring [16]. It employs a push-broom scanning technique for continuous spectral data acquisition and consists of two primary modules: the Fluorescence Imaging Spectrometer (FLUO) and the Reflectance Imaging Spectrometer (DUAL) [13]. The FLUO is specifically designed to capture spectral data in the 670–780 nm range, encompassing the two key chlorophyll fluorescence peaks at 687 nm (F687) and 760 nm (F760). Its fine spectral resolution of 0.25 nm enables accurate retrieval of SIF using methods such as the Fraunhofer Line Depth (FLD) [12]. The DUAL, on the other hand, covers a broader spectral range (400–2500 nm), providing critical reflectance information across the visible, near-infrared, and shortwave infrared regions.

The vegetation reflectance signal in the visible and near-infrared ranges (400–800 nm) has traditionally been exploited for retrieving the main photosynthetic pigments, such as chlorophylls and carotenoids. However, the full spectral range offers opportunities to more precisely disentangle pigment composition using spectral unmixing techniques.

Spectral unmixing has seen significant advances in recent years, driven by both methodological innovations and the increasing availability of high-dimensional hyperspectral data. Traditional unmixing approaches based on linear mixing models estimate

abundances but often fail with spectral variability and nonlinear interactions. Recent literature has focused on integrating spatial and spectral information, sparsity constraints, and machine learning to improve abundance estimation and robustness against noise and spectral variability. For instance, robust spatially regularized sparse unmixing frameworks with spectral library pruning have been proposed to mitigate spectral mismatch and noise effects in real hyperspectral datasets [17]. Deep learning methods, particularly autoencoder-based and transformer-style networks, have rapidly emerged, offering improved subpixel decomposition by jointly learning spectral representations and abundances with spatial context [18,19]. Comprehensive reviews highlight the transition from classical linear and nonlinear models to advanced machine learning and deep learning-based algorithms, underscoring ongoing challenges such as spectral variability, limited ground truth, and computational complexity [19,20]. These developments contextualise the need for unmixing strategies tailored to fluorescence and pigment absorption analysis in vegetation remote sensing, motivating our exploration of constrained and nonlinear unmixing formulations in airborne and proximal sensing data.

In addition to spectral unmixing, hyperspectral imagery has been successfully applied to a wide range of advanced remote sensing tasks leveraging machine learning and deep learning techniques. Modern transformer-based architectures, for example, have demonstrated state-of-the-art performance in hyperspectral image classification by integrating efficient dynamic token selection mechanisms to reduce computational redundancy while maintaining high accuracy, addressing the challenges of long-range spectral–spatial dependency modeling and computational cost [21]. Hybrid models that combine convolutional and transformer feature extractors have further enhanced classification performance by simultaneously capturing local texture and global context information [22]. Beyond classification, transformer-based frameworks have also been developed for hyperspectral target and point object detection, enabling precise identification of materials and small objects based on spectral signatures [23]. These applications demonstrate the versatility of hyperspectral data analysis across classification and detection domains, underscoring the broader impact of advanced modeling techniques in remote sensing beyond spectral unmixing.

Previous work [24] highlights the importance of refined remote sensing products by analysing, in greater detail, the photosynthetically absorbed photosynthetically active radiation (APAR) by fitting the absorption coefficients of individual pigments. That study introduced a non-negative least squares (NNLS) spectral unmixing algorithm to retrieve spectrally resolved effective absorbance factors for key pigments—Chlorophyll *a*, Chlorophyll *b*, *β*-Carotene, and xanthophylls—from reflectance data (500–780 nm). Among these, the effective absorbance factor of the primary photosynthetic pigment, Chlorophyll *a*, deserves particular attention.

To investigate energy partitioning and gain deeper insights into early stress detection in vegetation, the SIF can be normalised by the light absorbed by Chlorophyll *a*, yielding the fluorescence quantum efficiency (FQE) [24]. However, applying spectral fitting to the top-of the canopy reflectance signal requires that background signals—notably soil contributions—are taken into account [25].

A variety of models have been employed to address the spectral unmixing problem. For instance, Altmann et al. [26] proposed an unsupervised algorithm for nonlinear unmixing of hyperspectral images using a Gaussian process model to estimate abundance vectors across image pixels, and compared its performance with state-of-the-art techniques on synthetic data. Similarly, Halimi et al. [27] introduced a nonlinear bilinear model capable of capturing interactions among endmembers.

In this study, we extend the investigation of pigment effective absorbance spectral unmixing to airborne and proximal sensing data (HyPlant and FloX), considering both

linear and nonlinear approaches and accounting for the soil contribution as a background signal. To mitigate overfitting, we tested different physical constraints within the modeling framework, which includes the constrained least squares (CLS), potential function (POT), and bilinear (BIL) formulations described in the following sections. The pigment absorbance fitting models were applied to both airborne reflectance imagery and field spectroscopy data collected over a well-irrigated alfalfa crop throughout its growth cycle. The objective was to compare the retrieved effective absorbance of Chlorophyll *a* with the corresponding fluorescence quantum efficiency (FQE). We hypothesise that the effective absorbance of Chlorophyll *a* increases with crop development, as does the SIF, while the FQE remains relatively stable.

To clearly position this work within the existing literature, the main motivation of this study is to advance the interpretation of solar-induced chlorophyll fluorescence by linking it to physically meaningful pigment-level absorption processes, rather than relying solely on greenness-based or radiance-driven proxies of photosynthesis. While previous studies have demonstrated the potential of SIF as an indicator of photosynthetic activity, its interpretation remains challenged by variations in absorbed radiation, canopy structure, and background contributions. The key contribution of this manuscript is the extension and validation of pigment effective absorbance spectral unmixing approaches—previously demonstrated under controlled conditions—to airborne and proximal sensing observations, explicitly accounting for soil background effects and testing both linear and nonlinear mixing formulations. By jointly analysing HyPlant and FloX measurements over a crop growth cycle, this study provides a novel assessment of the relationship between Chlorophyll *a* effective absorbance and FQE at high spatial resolution. This framework enables a more physiologically grounded interpretation of SIF and contributes toward the development of next-generation remote sensing products aimed at monitoring actual photosynthetic performance and early stress detection in vegetation.

The paper is structured as follows. Section 2 details the materials and methods employed in the study, including a description of the field and airborne campaigns, the existing processing chains used, and the statistical models applied for the (f)APAR spectral unmixing strategy. Section 3 presents the results obtained using the proposed methodology, accompanied by their interpretation. In Section 4, a comprehensive discussion is provided, contextualizing the findings within the current state of the art. Finally, Section 5 summarizes the key conclusions of the study and outlines potential directions for future research in the discussed areas.

2. Materials & Methods

2.1. Experimental Site

The study site is located in northeastern Spain, within the Lleida region of the Ebro Basin, near the foothills of the Pyrenees (Figure 1). This area is geographically bounded by the Pyrenees to the north and the Iberian System to the south. The research focuses on a site west of Lleida, in the locality of La Cendrosa, where alfalfa (*Medicago sativa* L.) is the predominant crop. Figure 1 provides an overview of the study area, including a regional map and successive zooms highlighting the alfalfa field of interest. The region's characteristic Mediterranean climate, marked by hot, dry summers and mild, wet winters, offers optimal conditions for analysing vegetation dynamics and understanding crop–environment interactions. Field characterization for this study was conducted during an airborne campaign using the HyPlant sensor [12], complemented by ground-based measurements acquired with the FloX instrument [28].

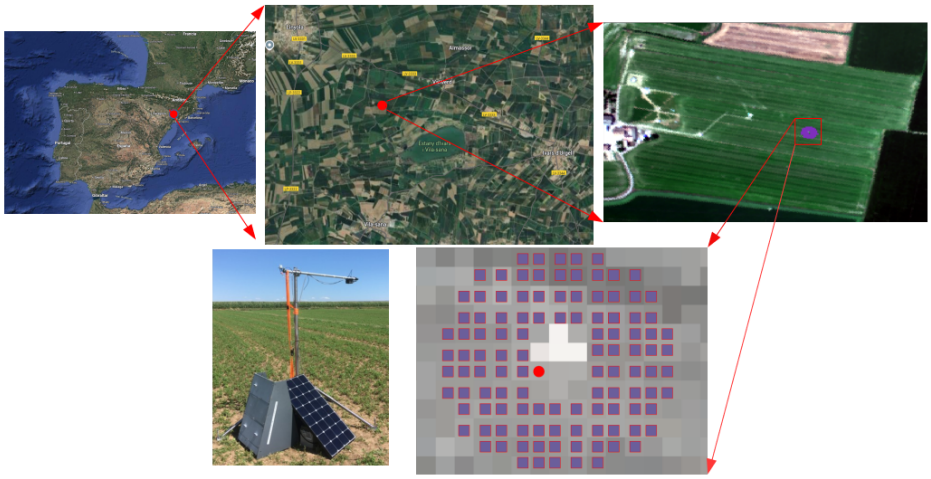

Figure 1. La Cendrosa field site in northeastern Spain with an alfalfa field. A HyPlant image is shown with 111 purple pixels (top-right), surrounding the FloX instrument. The bottom-down-left panel shows the FloX device in the field, while the bottom-right panel provides a close-up view of the FloX area, revealing individual pixels. The red dot marks the exact location of the FloX measurements, and the purple squares represent the 111 selected pixels used in the analysis.

2.2. Airborne Campaign and Preprocessed Products

2.2.1. Sensor and Campaign Overview

The HyPlant airborne imaging spectrometer was developed through a collaboration between Forschungszentrum Jülich (Germany) and the Finnish company SPECIM. Serving as the core reference instrument and technology demonstrator for the FLEX satellite mission, HyPlant is the first airborne sensor specifically designed to retrieve SIF [12].

HyPlant is a high-performance system composed of two integrated modules. The DUAL module contains two push-broom imaging spectrometers covering a wide spectral range (380–2500 nm). The FLUO module is dedicated to SIF measurements, acquiring data at high spectral resolution (0.25 nm) within the 670–780 nm range. Both modules are linked to an Oxford 3052 GPS/INS system. This synchronizes imaging data with precise aircraft position and orientation information, enabling accurate image rectification and georeferencing [13].

The flight campaign was conducted between 15 and 28 July 2021, covering over 100 flight lines. Data were acquired at 1150 m above ground level, between 13:00 and 17:00 local time. The datasets have a spatial resolution of 1.7 m $\times$ 1.7 m, a flight speed of 60 ft s^{-1}, and 20% overlap between adjacent lines to facilitate mosaic generation.

2.2.2. Spatial Sampling

For this study, we focused on a region of interest near the fixed sampling point for field spectroscopy. A total of 111 HyPlant pixels were selected for each flight day within a fixed radius from the centre of the FloX setup (Figure 1). Pixel selection was guided by: (1) proximity to the area captured by the sensor, (2) the dimensions of the FloX setup and its solar panels, ensuring only vegetation pixels comparable to point-fiber measurements were included, and (3) an appropriate radius reflecting the spectral representativity of the crop field. The spectral consistency among these pixels justifies the use of their mean spectrum for comparison with FloX measurements. As shown in Figure 2, both panel (a) reflectance and panel (b) absorbance demonstrate that the average spectrum is representative of the individual pixels.

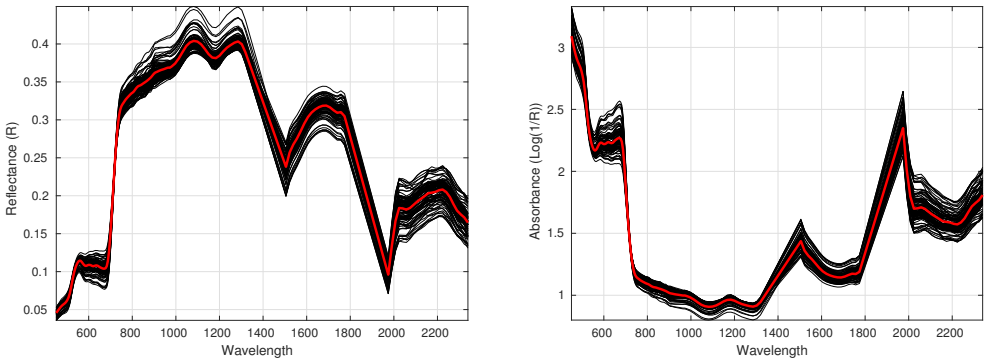

(**a**) (**b**)

Figure 2. (**a**) Spectral reflectance of 111 pixels extracted from the HyPlant image acquired on 15 July 2021. Red line is the averaged reflectance. (**b**) Corresponding absorbance spectra plotted on a logarithmic scale. Red line is the averaged absorbance. The high spectral consistency among these pixels supports using their mean spectrum for comparison with FLoX measurements.

2.2.3. TOC Reflectance and At-Surface Irradiance

Images from seven flight days (15, 16, 17, 20, 21, 22, and 27 July 2021) were processed. Raw HyPlant DUAL data were processed into top-of-canopy (TOC) reflectance using a multi-stage automated processing chain. First, raw DUAL image strips were radiometrically corrected at-sensor radiance using CaliGeoPRO software. During the same step, geometric lookup tables (GLTs) and MapLoc files were generated to support subsequent georeferencing. Atmospheric correction was then applied using the ATCOR algorithm (Atmospheric and Topographic CORrection) to transform at-sensor radiance into TOC radiance and reflectance. Following atmospheric correction, spectra were spectrally smoothed and distortions corrected. Finally, the products were georeferenced using the precalculated GLTs to generate flight lines and produce the final TOC reflectance.

While TOC radiance and reflectance derived from HyPlant DUAL data are standard products, the HyPlant FLUO module only provides at-sensor radiance without atmospheric correction. To retrieve at-surface irradiance, we used `libRadtran` [29,30] via the Atmospheric Look-up Table Generator software tool [31] (ALG, v1.2). ALG automates the generation of look-up tables (LUTs) for atmospheric radiative transfer models based on ranges of atmospheric and geometric variables, such as aerosol optical thickness, water vapor, solar and viewing angles, and atmospheric profiles. LUT nodes are generated using systematic or Latin Hypercube sampling.

For each node, the RTM computes atmospheric transfer functions, including path radiance, direct and diffuse irradiance at the surface, direct and diffuse transmittances to the sensor, and spherical albedo. These functions decouple atmospheric effects from the surface signal. Multidimensional interpolation of the LUTs enables application of atmospheric correction to measured data. In this study, all available atmospheric and geometric information (longitude, latitude, height, solar zenith angle, viewing zenith angle, solar and viewing azimuth angles, relative azimuth angle, roll, and pitch) was used for each flight day. Auxiliary data such as ozone concentration and aerosols were taken from the Copernicus Atmosphere Monitoring Service, which provides global reanalysis and near-real-time atmospheric data as part of the European Union's Copernicus Programme [32]. Based on these inputs, ALG returns the corresponding irradiance spectrum, which was then used for further analyses.

2.2.4. SIF at the O_2 Absorption Bands

The HyPlant airborne imaging spectrometer serves as the reference instrument and prime demonstrator for the FLEX satellite mission. HyPlant was the first airborne sensor optically optimized to image SIF by exploiting the two oxygen absorption features located at 687 nm (O_2-B) and 760 nm (O_2-A) in the electromagnetic spectrum. Since initial testing in 2012, research has confirmed the possibility of retrieving SIF in both the O_2-A and O_2-B bands [12].

The SIF products used in this study were obtained through the HyPlant processing chain, following the methodology described in the LIAISE campaign report [33]. The processing includes the radiometric calibration, atmospheric correction, geometric correction, and spectral extraction steps necessary to produce top-of-canopy SIF estimates. From these products, we derived spectrally-resolved fluorescence signals by emulating the retrieval of the fluorescence emission spectrum, as detailed in [34], through the ARTMO toolbox (https://artmotoolbox.com/, last accessed on 4 December 2025.).

For clarity and consistency, the SIF products are hereafter referred to using the following abbreviations: SIF_{O_2-A} and SIF_{O_2-B} for the fluorescence retrieved in the corresponding oxygen absorption bands, and SIF for the spectrally-resolved fluorescence signal. These abbreviations are used consistently in all figures, tables, and the workflow diagram to facilitate interpretation of the results.

2.3. Field Spectroscopy

To assess the quality of the HyPlant-derived SIF and spectral fitting products (e.g., SIF_{tot}, APAR-Chl*a*, and FQE), field measurements of incoming and reflected radiance were conducted using a point spectroradiometer, specifically a FloX system, installed at x m above the canopy. The FloX was positioned at a fixed location within the alfalfa field (0.93105°E, 41.69297°N) and operated continuously during the airborne campaigns on 15, 16, 17, 20, 21, 22, and 27 July 2021.

The FloX setup was optimized for continuous field monitoring under ambient sunlight, enabling high-temporal-resolution measurements of incoming and reflected radiance, which are critical for validating airborne observations. A consistent sampling strategy was employed, capturing data primarily during cloud-free periods to maximize the signal-to-noise ratio. For validation, FloX data acquired simultaneously with the HyPlant overpasses were selected for further processing. Table 1 summarizes the daily flight times for HyPlant and the corresponding closest measurements from the FloX sensor.

Table 1. Times of the HyPlant aircraft flights and the closest times in the FloX sensor data tables.

Day	Sensor	Start Time	Final Time
15	HyPlant, FloX	03:29:00 PM	04:22:00 PM
16	HyPlant, FloX	03:01:00 PM	03:52:00 PM
17	HyPlant, FloX	01:27:00 PM	02:19:00 PM
20	HyPlant, FloX	03:00:00 PM	03:51:00 PM
21	HyPlant, FloX	03:10:00 PM	04:02:00 PM
22	HyPlant, FloX	01:32:00 PM	02:26:00 PM
27	HyPlant	01:12:00 PM	02:02:00 PM

Spectrally resolved SIF retrievals were carried out using the SpecFit algorithm [35], which exploits the high spectral resolution of the instrument. This method provides robust estimates of top-of-canopy (TOC) reflectance and spectrally resolved fluorescence across the 680–780 nm range, enabling precise quantification of chlorophyll fluorescence dynamics.

HyPlant flight data were acquired at intervals of approximately one hour per flight. In this study, the 111-pixel subsets from each HyPlant image were compared with the temporally continuous FloX measurements. To ensure comparability, the same time window was selected for both sensors, aligning the static FloX measurements with the airborne snapshots.

2.4. Spectral Endmembers

A critical component of the proposed methodology is the definition and selection of spectral endmembers, particularly those representing pigment and background reflectance features. In this context, direct field measurements provide a reliable reference for the soil reflectance, which serves as the primary background component. Incorporating measured soil spectra enhances the robustness of the spectral unmixing procedure (see Section 2.5) and enables the evaluation of potential variations in model performance across different background conditions.

2.4.1. Soil Endmembers

To accurately characterise the soil background, 25 non-vegetated top-of-canopy (TOC) reflectance pixels were extracted from the HyPlant reflectance mosaic acquired on 15 July 2021. Figure 3 shows these 25 soil reflectance spectra (black lines), together with their mean spectrum (red line). Panel (a) presents the TOC reflectance (R) spectra, while panel (b) displays the corresponding apparent soil absorbance values, expressed as $\log(1/R)$. This logarithmic representation enhances contrast and facilitates a clearer identification of spectral features and absorption patterns.

The averaged soil spectrum was subsequently incorporated as a background endmember in the spectral unmixing models. All selected spectra correspond to bare soil pixels manually identified in the HyPlant scene, primarily located along field borders and near built-up areas. This selection provides a representative set of soil spectra suitable for use as reference background components in the unmixing analysis.

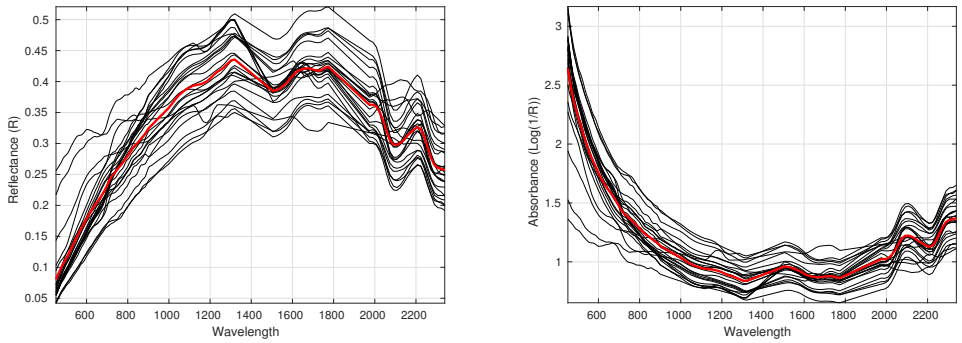

(**a**) (**b**)

Figure 3. (**a**) Spectral representation of 25 non-vegetated pixels extracted from the HyPlant reflectance image captured on 15 July 2021. These reflectance (R) spectra were selected from the HyPlant scene and include samples of bare soil. (**b**) Soil absorbance calculated as log(1/R).

2.4.2. Background and Pigment Bases

To apply the spectral unmixing approach to both the HyPlant and FLoX datasets, two distinct spectral bases were defined: a background basis and a pigment basis. The background basis combines synthetically generated spectra with the averaged soil reflectance spectrum derived from field measurements, ensuring realistic representation of non-vegetated background contributions.

The pigment basis comprises the principal photosynthetic and accessory pigments typically found in vegetation: Chlorophyll *a* (Chl.a), Chlorophyll *b* (Chl.b), *β*-Carotene (Car.b), Xanthophylls (Xan.a), and Anthocyanins (Anc). The corresponding absorption coefficients used as pigment endmembers are described in [24].

Figure 4 illustrates the two sets of endmembers employed in the spectral unmixing analysis. Panel (a) shows the background basis, including one endmember derived from the average of 25 non-vegetated pixels (see Section 2.4.1), complemented by four synthetically generated spectra that emulate the spectral behaviour of background surfaces. Panel (b) presents the pigment basis, displaying the characteristic absorbance spectra of Chl.a, Chl.b, Car.b, Xan.a, and Anc.

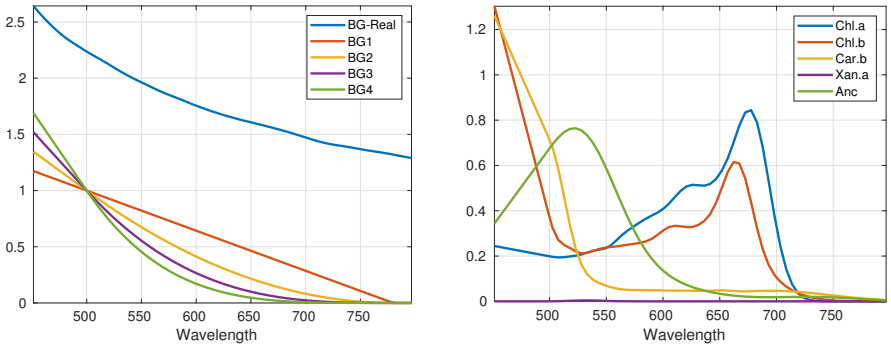

(**a**) (**b**)

Figure 4. Endmembers used in the spectral fitting with the background (BG) signals including the measured average soil absorbance obtained from the field (BG-Real) in panel (**a**), and the photosynthetic (Chl.a, Chl.b, Car.b, Xan.a) and non-photosynthetic (Anc) pigment absorbance coefficients in panel (**b**).

By jointly applying these two bases, the unmixing model effectively disentangles the spectral contributions of vegetation pigments and background signals, providing a more accurate interpretation of canopy optical properties and underlying biophysical processes.

The output parameters of the unmixing approach consist of the abundance weights assigned to each endmember and the corresponding effective absorbance values for the different spectral components. These parameters quantify the relative contributions of pigments and background reflectance within the observed spectra, providing valuable insights into canopy optical properties and supporting the refinement and validation of the spectral unmixing methodology.

2.5. Spectral NNLS Unmixing Framework for (f)APAR Components

In this study, both linear and non-linear spectral unmixing approaches were employed to retrieve the effective absorption coefficients of the selected components. The mathematical formulation of the unmixing framework and the definition of the endmember components are adapted from [24]. In essence, the effective absorption of each pigment or background component is expressed as the product of an abundance weight (w) obtained from the fitting process and the corresponding fixed endmember spectrum (400–780 nm) (Figure 4).

Several fitting strategies were implemented to evaluate model performance and physical consistency. To mitigate overfitting, physical constraints were introduced through a constrained least squares (CLS) formulation. In addition, two non-linear extensions were examined: a potential function (POT) model and a bilinear (BIL) model. This combination of approaches enables the identification of the most accurate and physically meaningful method for unmixing spectral signatures. Detailed descriptions of each model are provided in the following sections.

2.5.1. Constrained Least Squares (CLS) Model

Estimating spectral abundances can be formulated as a Constrained Least Squares (CLS) optimization problem [36]. While conventional Least Squares (LS) regression provides an optimal mathematical fit, it may yield abundance weights with negative values—lacking physical meaning in spectral decomposition—or fail to impose realistic constraints that prevent overfitting. The CLS formulation addresses these limitations by incorporating physically meaningful constraints that enforce non-negativity and improve the stability and interpretability of the solution.

Mathematically, the CLS problem can be expressed as a linear least-squares optimization with bound or linear constraints, ensuring that all estimated abundances remain within physically plausible ranges.

$$\alpha_{\mathrm{CLS}} = \arg\min_{\alpha \in \mathbb{R}^d} \frac{1}{2} \|B \cdot \alpha - p\|_2^2 \quad \text{subject to} \quad \begin{cases} B \cdot \alpha \leq p, \\ \alpha \geq 0. \end{cases} \tag{1}$$

In this formulation, the matrix B contains the endmember spectra as its columns, and the vector α represents the abundance weights (w) assigned to each endmember within the mixed pixel. In the CLS unmixing framework, the background matrix B includes both the real background spectrum (BG-Real) and synthetic background spectra, in addition to the pigment endmembers, to capture the full variability of the background signal. The CLS problem, as defined above, is a specific case of the more general constrained least squares formulation introduced by Lawson and Hanson [36], which can also incorporate equality constraints—though these are not required for the present study.

In our application, B corresponds to the combined pigment and background bases, while α denotes the estimated abundance weights for each component. The first constraint prevents overfitting by ensuring that the reconstructed spectrum ($B \cdot \alpha_{\mathrm{CLS}}$) does not exceed the observed pixel spectrum p, maintaining physical realism. The second constraint enforces non-negativity, ensuring that all abundance weights remain physically meaningful ($\alpha \geq 0$).

In addition to the CLS approach, we also consider non-linear unmixing models, as described in the following sections.

2.5.2. Potential Model

The first nonlinear approach introduces a potential function based on the abundance weights obtained from the CLS solution. This model aims to capture potential nonlinearities between the fitted spectra and the observed signal. It is implemented in two steps: first, solving the optimization problem defined in Equation (2), and second, retrieving the scalar potential value $s \in \mathbb{R}$ that minimizes the reconstruction error. The optimization problem is formulated as:

$$\arg\min_{s \in \mathbb{R}} \frac{1}{2} \left\| (B \cdot \alpha_{\mathrm{CLS}})^s - p \right\|_2^2, \tag{2}$$

where s acts as a global potential exponent that modulates the contribution of the linearly mixed components. This formulation allows the model to flexibly adjust the nonlinearity degree between the reconstructed and observed spectra, potentially improving the fit for complex canopy or background interactions.

2.5.3. Bilinear Model

The second nonlinear model considered in this study is the Bilinear (BIL) model, widely used in previous hyperspectral unmixing studies [27,37]. The BIL model extends the linear mixing framework by incorporating second-order interaction terms between

different endmembers, accounting for multiple scattering or mutual photon interactions within a mixed pixel.

The observed pixel spectrum p is modeled as:

$$p = B\alpha + \sum_{i=1}^{d-1} \sum_{j=i+1}^{d} \beta_{i,j}\, m_i \odot m_j, \tag{3}$$

where the first term ($B\alpha$) represents the linear contribution of each endmember, and the second term captures nonlinear interactions between endmembers m_i and m_j. The operator $\odot$ denotes the Hadamard (element-wise) product, and $\beta_{i,j}$ quantifies the strength of the interaction between endmembers i and j. Additive noise is typically assumed to be Gaussian with zero mean and fixed variance.

To efficiently represent the interaction terms, we define a mapping function ψ as:

$$\begin{aligned} \psi :\ & \mathbb{R}^d \to \mathbb{R}^{\frac{d(d-1)}{2}}, \\ & a \mapsto \psi[a] = [a_1, a_2, \ldots, a_d, a_1a_2, \ldots, a_1a_d, a_2a_3, \ldots, a_{d-1}a_d]^T, \end{aligned} \tag{4}$$

which encodes both the original abundance weights and all pairwise interaction terms present in Equation (3). This mapping allows the bilinear model to be reformulated in a vectorized form, facilitating its numerical implementation and optimization.

2.6. Airborne Versus Ground-Based Retrieval of APAR$_{Chl\ a}$ and FQE

After evaluating and comparing the different spectral fitting strategies described in Section 2.5, a consistent retrieval approach was applied to both the airborne HyPlant data and the ground-based FloX measurements for all campaign days, as illustrated in the workflow diagram (Figure 5). This harmonized framework allows for a direct comparison of the absorbed photosynthetically active radiation associated with chlorophyll *a* (APAR$_{\text{Chl a}}$) and the fluorescence quantum efficiency (FQE) derived from each platform.

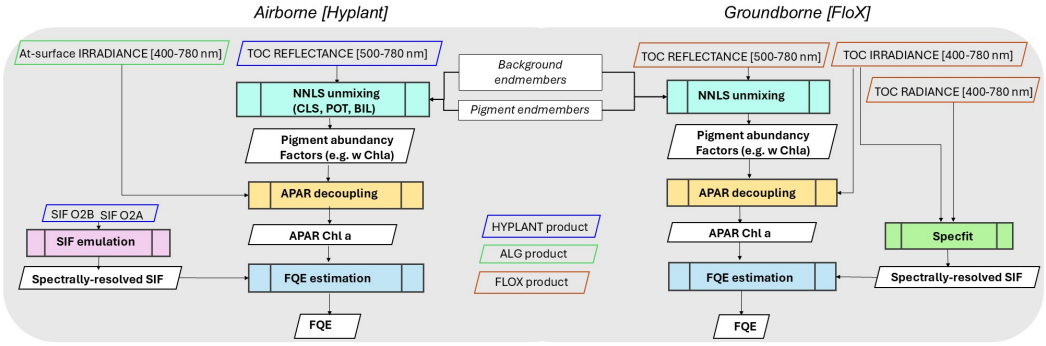

Figure 5. Workflow for the HyPlant and FLoX datasets. Input products obtained from existing processing chains are shown in grey boxes with coloured borders, while white boxes represent the products generated in this study following the pigment fitting approach. The variable w Chla denotes the abundance weight assigned to chlorophyll *a* by the spectral unmixing model, from which the absorbed photosynthetically active radiation (APAR) and fluorescence quantum efficiency (FQE) are derived.

APAR$_{\text{Chl a}}$ was computed for both datasets based on the fAPAR$_{\text{Chl a}}$ obtained from the spectral unmixing model, combined with the incoming irradiance within the photosynthetically active region (450–800 nm). Mathematically, this can be expressed as $\text{APAR Chl a}(\lambda) = w_{\text{Chl a}}\text{Chl a}(\lambda) \cdot \text{PAR}(\lambda)$, where $\text{PAR}(\lambda)$ stands for the surface irradiance for each $\lambda \in [450, 800]$ nm.

$$\text{Total APAR}_{\text{Chl a}} = \int_{450}^{800} \text{APAR Chl a}(\lambda)\, d\lambda, \tag{5}$$

where $E_{\text{in}}(\lambda)$ represents the spectral downwelling irradiance at the canopy top. This formulation ensures that the absorbed fraction of photosynthetically active radiation is directly linked to the chlorophyll abundance retrieved from the spectral unmixing framework. The 450–800 nm range was chosen to encompass the primary absorption bands of chlorophyll a, including the blue (450–500 nm) and red (650–700 nm) peaks, as well as the far-red region relevant for fluorescence. While the classical PAR range is 400–700 nm, this extended range allows for more accurate estimation of $\text{APAR}_{\text{Chl a}}$ and its combination with SIF for FQE calculation.

The fluorescence quantum efficiency (FQE) was derived as the ratio between the total spectrally integrated sun-induced fluorescence emission (SIF_{tot}) and the spectrally integrated absorbed energy by chlorophyll *a*, and is given by

$$\text{FQE} = \frac{\int_{\lambda_1}^{\lambda_2} SIF(\lambda)\, d\lambda}{\text{Total APAR}_{\text{Chl a}}}, \tag{6}$$

where λ_1 and λ_2 correspond to the spectral range of the retrieved fluorescence emission (e.g., 650–800 nm). This ratio provides a quantitative measure of the efficiency of fluorescence emission relative to the absorbed energy by chlorophyll *a*.

The spectrally integrated fluorescence emission used in the FQE calculation was obtained using methods tailored to each dataset. For the HyPlant airborne data, the SIF products were derived through the HyPlant fluorescence processing chain, employing a spectral emulation technique that reconstructs high-resolution SIF spectra from the O_2-A and O_2-B bands. For the ground-based FloX measurements, SIF retrieval was performed using the SpecFit method, which fits the observed radiance in the oxygen absorption bands to estimate spectrally resolved fluorescence under field conditions. By applying these complementary approaches, we ensured a robust comparison between airborne and ground-based observations, allowing for consistent retrievals of $\text{APAR}_{\text{Chl a}}$ and FQE across different spatial and temporal scales. Based on this dataset, we hypothesize that crop growth is associated with an increase in the effective absorbance of chlorophyll *a* and in sun-induced fluorescence, while the fluorescence quantum efficiency (FQE) exhibits minimal variation.

3. Results

3.1. Spectral Pigment and Background Unmixing

We begin by evaluating the performance of the three spectral unmixing models described in Section 2.5: Constrained Least Squares (CLS), the Potential function model (POT), and the Bilinear model (BIL). Each model presents distinct advantages and limitations, which will be discussed in detail. Based on this comparative analysis, a final model will be selected for subsequent analyses.

Following the model selection, we present the core findings of this study, focusing on the comparison between the spectral unmixing results obtained from airborne HyPlant imagery and those derived from ground-based FloX measurements. This comparison provides a critical assessment of the consistency and reliability of the retrieved pigment abundances and associated functional parameters across platforms.

Figure 6 presents the average spectral fitting results for 111 HyPlant pixels across all seven campaign days. Rows correspond to the three unmixing models (CLS, POT, and BIL). Each panel shows the measured spectra, the spectra reconstructed by the models, and the

weighted contributions of the spectral basis, providing a clear visualization of the influence of each endmember on the fitted results.

The RMSE values shown in Figure 7 exhibit distinct peaks for each model. The CLS model displays higher RMSE values around 500 nm, 600 nm, 650 nm, and 700 nm. The POT model exhibits a pronounced peak near 700 nm, with lower values outside this range but also several smaller peaks. The BIL model shows a prominent peak at 700 nm, followed by a secondary peak at 650 nm.

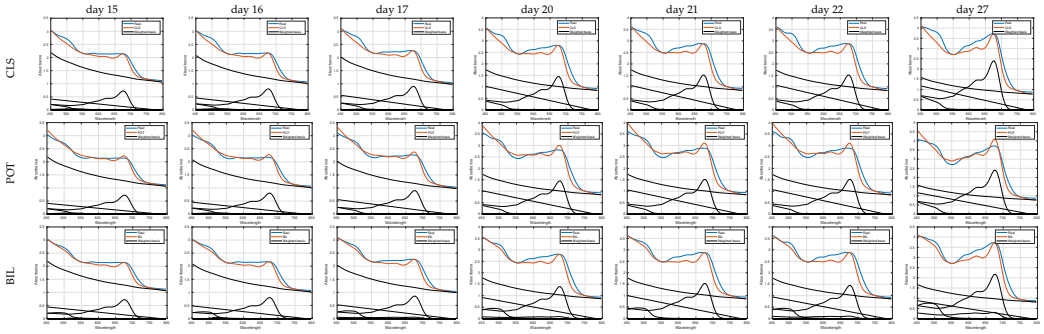

Figure 6. Spectral fitting results for the mean of 111 HyPlant pixels across the seven campaign days. Rows correspond to the three unmixing models (CLS, POT, and BIL), while columns represent individual days of the study.

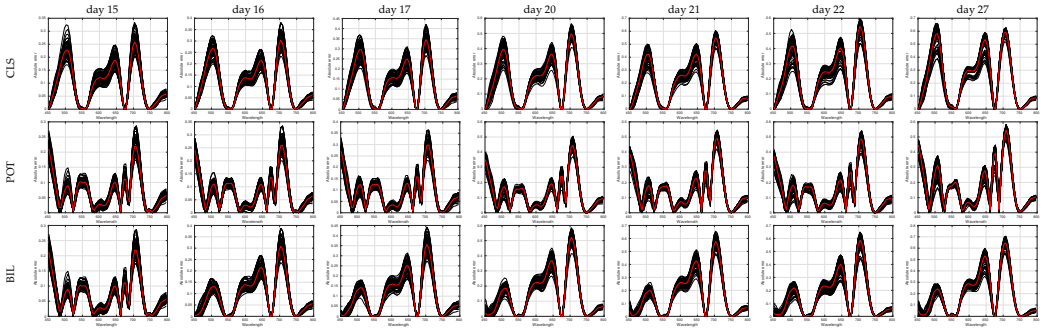

Figure 7. RMSE of spectral fitting for a subset of 111 HyPlant pixels. Rows correspond to the three unmixing models (CLS, POT, and BIL), and columns correspond to each campaign day. Red line represents the average.

These peaks indicate the wavelengths where the models have greater difficulty accurately fitting the observed spectra, likely due to increased variability or noise in the data. The recurring peaks around 700 nm, in particular, highlight a shared challenge among all models, potentially associated with spectral features of chlorophyll and other pigments. Understanding these regions of higher error is crucial for assessing the effectiveness of each fitting method in capturing the spectral characteristics of the observed phenomena. The RMSE peak at 700–720 nm likely reflects chlorophyll's spectral features, the rigid shapes of the absorption coefficients, and possible fluorescence re-absorption; however, its impact on the overall FQE calculation is limited due to integration over a broader spectral range.

Overall, the Potential Function (POT) model achieves the lowest RMSE between the reconstructed spectra and the HyPlant input data, as illustrated in Figure 7. However, this method is prone to overfitting, often producing solutions that are physically implausible or inconsistent. In contrast, the Constrained Least Squares (CLS) and Bilinear (BIL) models yield slightly higher reconstruction errors but effectively constrain the solutions, preventing overfitting and demonstrating more robust modeling behavior. Considering the balance between reconstruction accuracy, physical plausibility, and model simplicity, the CLS method is recommended for the subsequent analyses. The POT and BIL formulations allow

greater flexibility in fitting the data, which can lead to overfitting of noise or minor spectral variability, resulting in abundance estimates that are physically implausible.

3.2. fAPAR Chlorophyll a Based on CLS Spectral Fitting

The CLS-based pigment absorbance fitting models were applied to both airborne reflectance imagery and field spectroscopy data as outlined in Figure 5, with the aim to compare the obtained effective absorbance by Chlorophyll *a* on the one hand, and the fluorescence quantum yield (FQE) on the other hand. The abundance weights $w_{\text{Chl a}}$ and rsulting $\text{fAPAR}_{\text{Chl a}}$ retrieved from HyPlant and FloX data exhibited consistent temporal trends throughout the campaign (Figure 8). Specifically, the HyPlant-derived $\text{fAPAR}_{\text{Chl a}}$ showed increasing values from first to last days, closely matching the values obtained from the FloX measurements, which served as a temporal-resolution ground reference (Figure 8). The comparison indicates strong agreement between airborne and ground-based retrievals, with minor deviations attributable to differences in spatial resolution and canopy heterogeneity.

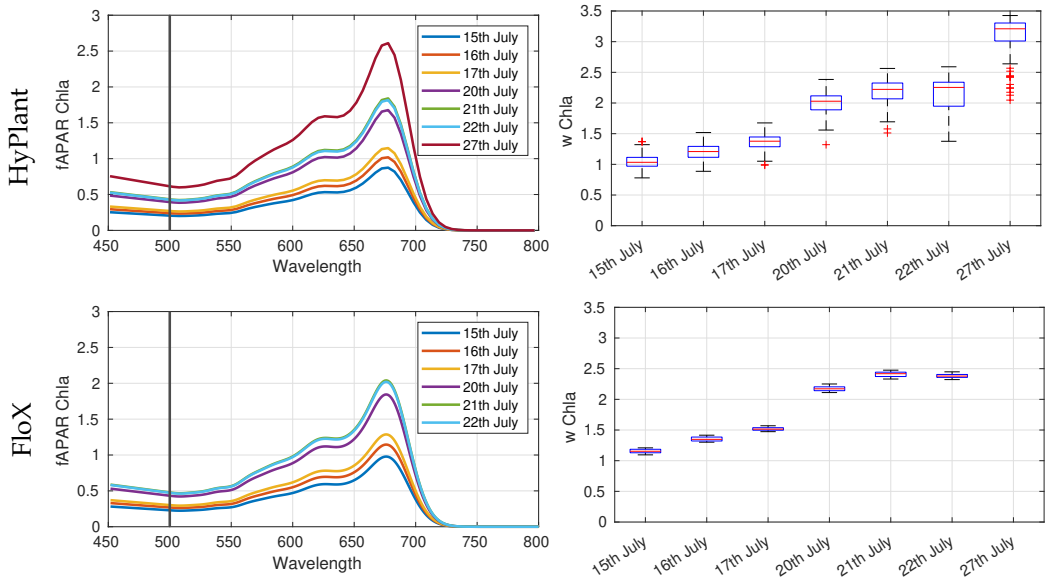

Figure 8. Results of the CLS-based pigment unmixing approach for HyPlant (**up**) and FloX (**down**) datasets: $\text{fAPAR}_{\text{Chl a}}$ (**left**) and abundance weights $w_{\text{Chl a}}$ (**right**) obtained along the experiment. HyPlant results show the mean fitting result for 111 pixels. Note that the obtained $\text{fAPAR}_{\text{Chl a}}$ is shown for the fitted range 500–780 nm, while it is obtained for the full PAR range.

3.3. APAR Chl, Spectrally-Resolved SIF and FQE

The spectrally-integrated SIF, obtained using the emulation technique on fluorescence retrieved in the O_2-A and O_2-B bands for HyPlant, and using the SpecFit method for FloX, followed a similar increasing pattern to $\text{fAPAR}_{\text{Chl a}}$.

Figure 9 presents an overview of $\text{APAR}_{\text{Chl a}}$ and spectrally resolved SIF derived from HyPlant and FloX measurements over the alfalfa field. The spatial patterns reveal substantial variability in both parameters, primarily driven by differences in canopy structure and pigment distribution. Regions with higher chlorophyll absorption generally coincide with increased SIF emission, emphasizing the strong coupling between absorbed photosynthetically active radiation and fluorescence output. Furthermore, the FQE, defined as the ratio of integrated SIF to integrated $\text{APAR}_{\text{Chl a}}$, remained relatively stable across all observation dates. This stability supports the hypothesis that the efficiency of fluorescence emission does not exhibit significant variation during the monitored growth period.

Figure 10 presents the SIF_{tot}, calculated according to the expression provided in the numerator of Equation (6). The first three acquisition days (15th, 16th, and 17th) display

slightly noisier spatial patterns compared with the remaining days of the study. In contrast, the days following to the 17th exhibit more homogeneous spatial structures, suggesting a more uniform photosynthetic performance of the investigated alfalfa variety.

Figure 11 shows the spatial distribution of FQE for each pixel across the seven HyPlant acquisition days. For consistency, the FQE color scale ranges from 0 to 0.05 in all panels. Urban areas and roads were masked prior to analysis to avoid non-vegetated contributions. On the first day (15th), FQE values are generally lower and more spatially homogeneous. In contrast, the 16th and 17th exhibit the highest FQE levels, although the patterns appear noisier and less spatially coherent. During the remaining days, intermediate FQE values dominate, displaying more structured and stable spatial patterns with no pronounced day-to-day changes. This progression reflects both short-term variability and the overall stability of the canopy physiological status during the study period. Moreover, the FQE remained almost constant because the alfalfa crop was observed during a period in which plants were not experiencing strong physiological stress. Alfalfa is a resilient, well-adapted crop, and the field conditions during our observations did not induce substantial variations in chlorophyll content or other physiological traits that would be expected to affect fluorescence efficiency.

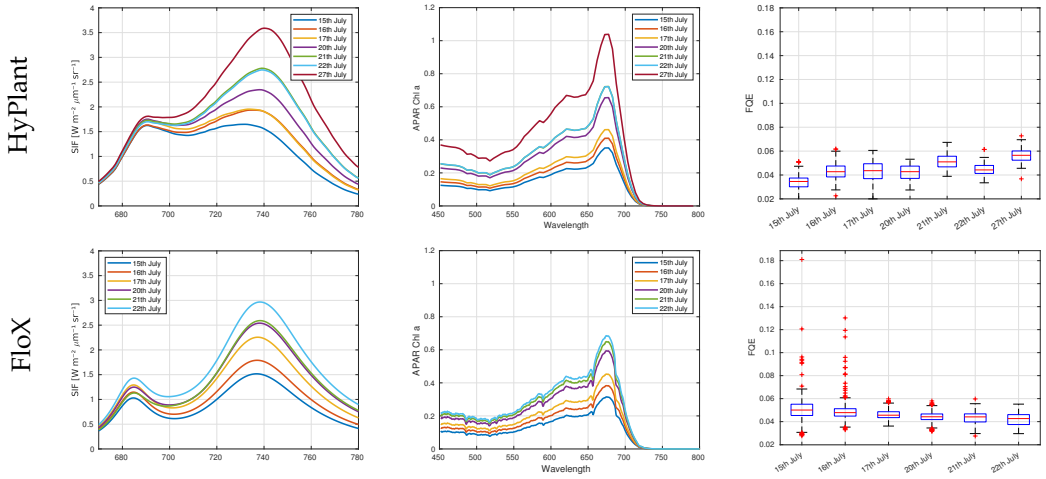

Figure 9. Sun induced fluorescence (**first column**), spectrally-resolved APAR Chl a (400–780 nm) averaged values from the 111 HYPLANT pixels and for the FloX instrument (**second column**), and FQE calculated from the spectrally integrated results of the previous entries (**third column**).

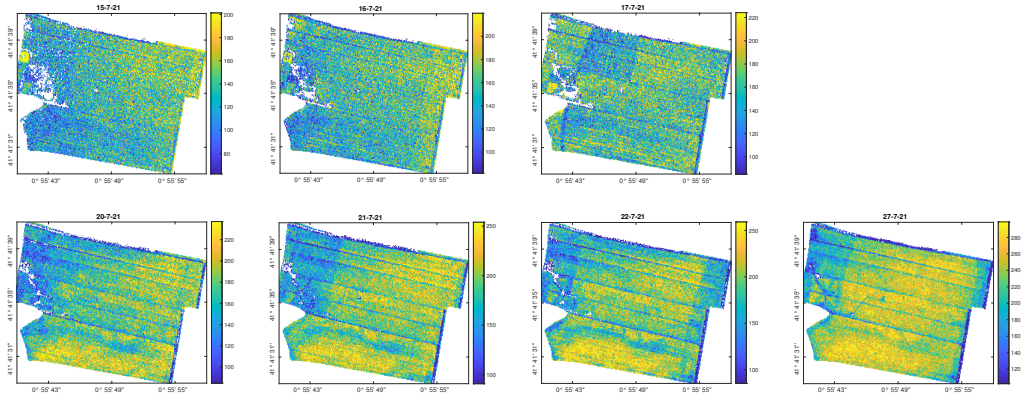

Figure 10. SIF_{tot} values for each pixel in the seven HyPlant maps. The date for each map is shown as the title of its corresponding plot (day/month/year).

Figure 12 illustrates the FQE values for each pixel across the seven HyPlant maps used in this study. The SIF values were emulated following the methodology proposed in [34]. It is important to recall that HyPlant acquires SIF only in the O_2-A and O_2-B bands;

therefore, to generate the full set of plots shown here, it is necessary to emulate SIF values as done in previous related work [38]. Overall, the spatial structure within each map (Figure 11) is consistent and well defined, revealing homogeneous patterns that suggest spatially coherent photosynthetic performance of the investigated alfalfa variety. Only the maps from the 16th and 17th July days exhibit noticeable noisy values. Furthermore, FQE does not appear to vary substantially across the acquisition dates. This observation is also supported by Figure 12, which presents the pixel-level boxplots for each day included in the study.

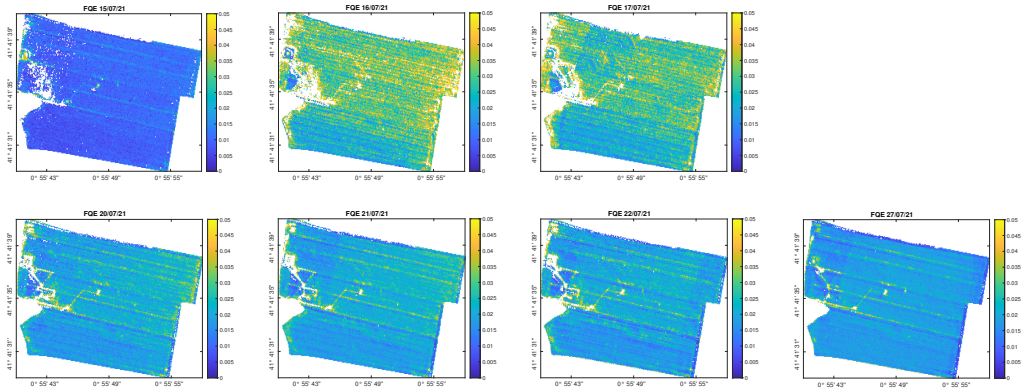

Figure 11. FQE values for each pixel in the seven HyPlant maps. The date for each map is shown as the title of its corresponding plot (day/month/year).

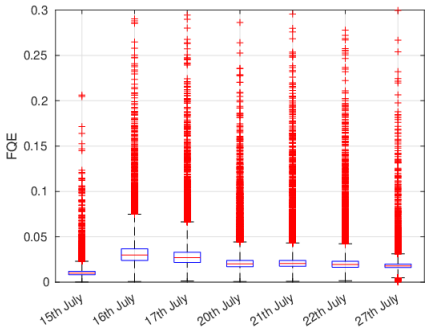

Figure 12. FQE boxplot values for each pixel in the seven HyPlant maps. This plot was computed from the maps reported at Figure 11.

4. Discussion

By applying pigment-based spectral unmixing and subsequent fluorescence modeling, we were able to retrieve the effective absorbance fraction of chlorophyll *a* (fAPAR Chl *a*) that followed the trend of crop growth of the alphalpha field. In agreement with previous studies [38–40], the magnitude of Sun-Induced Fluorescence radiance was found to be primarily driven by the pattern of photosynthetically active radiation (Figure 9).

After normalization of the fluorescence emission by the respective effective absorbance of chlorophyll *a* (APAR Chl *a*), a more stable trend of FQE along the flight days was obtained. The spectral fitting approach using the Constrained Least Squares (CLS) model provided stable and physically interpretable estimates of pigment abundances, which were consistent across the HyPlant imagery and the ground-based FloX measurements. This methodological consistency allowed for direct comparison between scales, demonstrating that the retrieved APAR Chl *a* values increased with canopy development, while the FQE remained relatively stable—indicating a balanced photosynthetic efficiency under well-irrigated conditions.

The comparison between HyPlant and FloX datasets further confirmed the robustness of the proposed approach: both platforms captured similar trends, with consistent increases in effective chlorophyll absorption during crop growth and stable FQE dynamics throughout the observation period. These results reinforce the potential of combining spectral unmixing with high-resolution SIF measurements to disentangle structural and functional drivers of canopy fluorescence, even without resorting to full radiative transfer simulations. Other approaches to normalize the emission of SIF have been proposed, but focused on the O2A-band fluorescence F760 so far only. For example, Bendig et al. [41] evaluated two normalization strategies to correct diurnal TOC SIF observations in summer barley for structural and environmental confounding effects. Using both airborne and drone-based spectrometers, the study compared the fluorescence correction vegetation index (FCVI) with three variants of the near-infrared reflectance of vegetation (NIRv). Radiative transfer simulations with DART confirmed that NIRvH1 outperformed the other methods, closely reproducing modeled chlorophyll F760 emission efficiency ($R^2 = 0.99$). Using a spectral fitting method over an index to obtain efficiency contains however the possibility to resolve the entire photosynthetic range for structural effects related to both fCOVER and vertical canopy structure scattering effects. While the first structural effect (spatial fCOVER) is addressed by the incorporation of a soil endmember, the second structural effect (multiple scattering within the canopy) was addressed by the attempt to account for non-linear behaviour of the pigment endmember fitting functions (a potential function and a bilinear model). While all fitting methods (CLS, POT, BIL) could account well for the soil absorbance effects, the nonlinear extensions of the CLS method did not improve substantially the fitting result (Figure 7). The fitting error observed slightly reduced for the potential fitting, but however kept around 0.2 absolute error for the red-edge region (690–710 nm). Similar absolute error fitting shapes were observed after applying the CLS method for leaf level data [24], pointing to a need for improving pigment endmember behaviour.

Data from the HyPlant flights acquired at approximately 680 m above ground level exhibited a notable degree of variability, in line with previous findings by [41,42]. Throughout the measurement period, the top-of-canopy fluorescence at 760 nm (F760) followed the expected pattern. However, the observed decline in F760 was relatively small. This attenuated decrease can be attributed to the advanced developmental stage of the alfalfa canopy during the observation campaign, as mature and structurally dense canopies typically exhibit a more stable fluorescence response under high-light conditions [43]. Similar patterns have been reported by [42], who found a more pronounced afternoon decrease in F760 for crops at earlier phenological stages, suggesting that canopy maturity and structure strongly modulate the diurnal variability of SIF signals.

5. Conclusions & Future Work

This study demonstrates the feasibility and effectiveness of combining airborne hyperspectral imagery (HyPlant) with ground-based field spectroscopy (FloX) to retrieve pigment-specific effective absorbance, Sun-Induced Chlorophyll Fluorescence (SIF), and fluorescence quantum efficiency (FQE) in an alfalfa crop. Using spectral unmixing approaches, including Constrained Least Squares (CLS), Potential Function (POT), and Bilinear (BIL) models, we were able to disentangle pigment and background contributions in the top-of-canopy reflectance, while attempting to account for the non-linear absorption effects in the canopy.

The CLS model proved to be the most robust, providing a good reconstruction of the observed spectra while avoiding overfitting, whereas POT and BIL offered insights into nonlinear interactions but sometimes produced physically implausible solutions. The derived $fAPAR_{Chl\ a}$ and spectrally-integrated SIF were successfully combined to calculate FQE, showing strong consistency between airborne and ground-based measurements.

These results highlight the potential of advanced spectral unmixing frameworks for accurately quantifying pigment absorption and fluorescence at both local and field scales. The methodology presented here can support high-resolution monitoring of photosynthetic performance and early detection of vegetation stress, providing a reliable pathway for precision agriculture and ecosystem research.

Future research should aim to extend the spectral unmixing framework to a broader range of ecosystems and canopy architectures, including heterogeneous and forested environments, to assess the scalability and robustness of the proposed approach. Also, further finetuning of the endmember absorption shapes is proposed. Incorporating temporal dynamics through time-series analysis would also provide valuable insights into the evolution of photosynthetic efficiency and pigment composition under varying environmental conditions. Furthermore, the integration of machine learning or hybrid physical–statistical models could enhance the retrieval accuracy of pigment absorption and fluorescence parameters from hyperspectral data. The upcoming FLEX mission and concurrent imaging spectroscopy platforms will offer unique opportunities to validate and refine the presented methods at regional and global scales, ultimately contributing to improved monitoring of vegetation health and early stress detection in both natural and agricultural systems.

Author Contributions: Conceptualization, S.V.W. and A.B.P.-V.; methodology, A.B.P.-V. and A.P.-S.; software, A.B.P.-V. and A.P.-S.; validation, A.B.P.-V., M.P.C.-M. and S.V.W.; formal analysis, A.M.; investigation, A.B.P.-V.; resources, M.M. and J.V.S.; data curation, B.S.; writing—original draft preparation, A.B.P.-V.; writing—review and editing, S.V.W. and A.P.-S.; visualization, B.S.; supervision, S.V.W.; project administration, S.V.W.; funding acquisition, S.V.W. All authors have read and agreed to the published version of the manuscript.

Funding: Bastian Siegmann acknowledge the financial support of the French National Agency for Research (CNRS) (grant number ANR-19-01CE-0017 in support of the project "HILIAISE: Human Imprint on Land surface Interactions with the Atmosphere over the Iberian Semi-arid Environment") that funded the field and airborne data acquisition. SVW, AM and ABP and this work were further supported by the European Research Council (ERC) under the ERC-2021-STG project PHOTOFLUX (grant agreement no. 101041768).

Institutional Review Board Statement: Not applicable.

Informed Consent Statement: Not applicable.

Data Availability Statement: Restrictions apply to the datasets.

Conflicts of Interest: Author Bastian Siegmann was employed by the company Forschungszentrum Jülich GmbH. The remaining authors declare that the research was conducted in the absence of any commercial or financial relationships that could be construed as a potential conflict of interest.

References

1. Eng, D.; Baranoski, G.V.G. The Application of Photoacoustic Absorption Spectral Data to the Modeling of Leaf Optical Properties in the Visible Range. *IEEE Trans. Geosci. Remote Sens.* **2007**, *45*, 4077–4086. [CrossRef]
2. Mohammed, G.H.; Colombo, R.; Middleton, E.M.; Rascher, U.; van der Tol, C.; Nedbal, L.; Goulas, Y.; Pérez-Priego, O.; Damm, A.; Meroni, M.; et al. Remote sensing of solar-induced chlorophyll fluorescence (SIF) in vegetation: 50 years of progress. *Remote Sens. Environ.* **2019**, *231*, 111177. [CrossRef] [PubMed]

3. Monteith, J.L. Solar Radiation and Productivity in Tropical Ecosystems. *J. Appl. Ecol.* **1972**, *9*, 747–766. [CrossRef]
4. Zheng, B.; Ciais, P.; Chevallier, F.; Yang, H.; Canadell, J.G.; Chen, Y.; van der Velde, I.R.; Aben, I.; Chuvieco, E.; Davis, S.J.; et al. Record-high CO_2 emissions from boreal fires in 2021. *Science* **2023**, *379*, 912–917. [CrossRef] [PubMed]
5. Porcar-Castell, A.; Tyystjärvi, E.; Atherton, J.; van der Tol, C.; Flexas, J.; Pfündel, E.E.; Moreno, J.; Frankenberg, C.; Berry, J.A. Linking chlorophyll a fluorescence to photosynthesis for remote sensing applications: Mechanisms and challenges. *J. Exp. Bot.* **2014**, *65*, 4065–4095. [CrossRef]
6. Drusch, M.; Moreno, J.; Del Bello, U.; Franco, R.; Goulas, Y.; Huth, A.; Kraft, S.; Middleton, E.M.; Miglietta, F.; Mohammed, G.; et al. The FLuorescence EXplorer Mission Concept-ESA's Earth Explorer 8. *IEEE Trans. Geosci. Remote Sens.* **2017**, *55*, 1273–1284. [CrossRef]
7. Berger, K.; Machwitz, M.; Kycko, M.; Kefauver, S.C.; Van Wittenberghe, S.; Gerhards, M.; Verrelst, J.; Atzberger, C.; van der Tol, C.; Damm, A.; et al. Multi-sensor spectral synergies for crop stress detection and monitoring in the optical domain: A review. *Remote Sens. Environ.* **2022**, *280*, 113198. [CrossRef]
8. Kaufmann, H.; Segl, K.; Guanter, L.; Hofer, S.; Foerster, K.P.; Stuffler, T.; Mueller, A.; Richter, R.; Bach, H.; Hostert, P.; et al. Environmental Mapping and Analysis Program (EnMAP) - Recent Advances and Status. In Proceedings of the IGARSS 2008—2008 IEEE International Geoscience and Remote Sensing Symposium, Boston, MA, USA, 7–11 July 2008; Volume 4, pp. IV-09–IV-112. [CrossRef]
9. Pignatti, S.; Palombo, A.; Pascucci, S.; Romano, F.; Santini, F.; Simoniello, T.; Umberto, A.; Vincenzo, C.; Acito, N.; Diani, M.; et al. The PRISMA hyperspectral mission: Science activities and opportunities for agriculture and land monitoring. In Proceedings of the 2013 IEEE International Geoscience and Remote Sensing Symposium—IGARSS, Melbourne, VIC, Australia, 21–26 July 2013; pp. 4558–4561. [CrossRef]
10. Moreno, J.F. Advances in the Retrieval and Interpretation of Solar-Induced Vegetation Chlorophyll Fluorescence Using Passive Remote Sensing Techniques. In Proceedings of the 2021 IEEE International Geoscience and Remote Sensing Symposium IGARSS, Brussels, Belgium, 11–16 July 2021; pp. 1915–1918. [CrossRef]
11. Guanter, L.; Zhang, Y.; Jung, M.; Joiner, J.; Voigt, M.; Berry, J.A.; Frankenberg, C.; Huete, A.R.; Zarco-Tejada, P.; Lee, J.E.; et al. Global and time-resolved monitoring of crop photosynthesis with chlorophyll fluorescence. *Proc. Natl. Acad. Sci. USA* **2014**, *111*, E1327–E1333. [CrossRef]
12. Rascher, U.; Alonso, L.; Burkart, A.; Cilia, C.; Cogliati, S.; Colombo, R.; Damm, A.; Drusch, M.; Guanter, L.; Hanus, J.; et al. Sun-induced fluorescence—A new probe of photosynthesis: First maps from the imaging spectrometer HyPlant. *Glob. Change Biol.* **2015**, *21*, 4673–4684. [CrossRef]
13. Siegmann, B.; Alonso, L.; Celesti, M.; Cogliati, S.; Colombo, R.; Damm, A.; Douglas, S.; Guanter, L.; Hanuš, J.; Kataja, K.; et al. The High-Performance Airborne Imaging Spectrometer HyPlant—From Raw Images to Top-of-Canopy Reflectance and Fluorescence Products: Introduction of an Automatized Processing Chain. *Remote Sens.* **2019**, *11*, 2760. [CrossRef]
14. Cook, B.; Corp, L.; Clemens, P.; Paynter, I.; Nagol, J.; McCorkel, J. Characterization of Firefly, an Imaging Spectrometer Designed for Airborne Measurements of Solar-Induced Fluorescence. In Proceedings of the IGARSS 2018—2018 IEEE International Geoscience and Remote Sensing Symposium, Valencia, Spain, 22–27 July 2018; pp. 3943–3946. [CrossRef]
15. Frankenberg, C.; Köhler, P.; Magney, T.S.; Geier, S.; Lawson, P.; Schwochert, M.; McDuffie, J.; Drewry, D.T.; Pavlick, R.; Kuhnert, A. The Chlorophyll Fluorescence Imaging Spectrometer (CFIS), mapping far red fluorescence from aircraft. *Remote Sens. Environ.* **2018**, *217*, 523–536. [CrossRef]
16. Cogliati, S.; Rossini, M.; Julitta, T.; Meroni, M.; Schickling, A.; Burkart, A.; Pinto, F.; Rascher, U.; Colombo, R. Continuous and long-term measurements of reflectance and sun-induced chlorophyll fluorescence by using novel automated field spectroscopy systems. *Remote Sens. Environ.* **2015**, *164*, 270–281. [CrossRef]
17. Zhang, S.; Liu, Y.; Li, F.; Zheng, J.; Lai, P.; Deng, C.; Tang, M.; Wang, S. Robust spatially regularized sparse unmixing of hyperspectral remote sensing images with spectral library pruning. *Infrared Phys. Technol.* **2025**, *145*, 105697. [CrossRef]
18. Zhang, M.; Yang, M.; Xie, H.; Yue, P.; Zhang, W.; Jiao, Q.; Xu, L.; Tan, X. A Global Spatial-Spectral Feature Fused Autoencoder for Nonlinear Hyperspectral Unmixing. *Remote Sens.* **2024**, *16*, 3149. [CrossRef]
19. Zou, J.; Qu, H.; Zhang, P. Conventional to Deep Learning Methods for Hyperspectral Unmixing: A Review. *Remote Sens.* **2025**, *17*, 2968. [CrossRef]
20. Rasti, B.; Zouaoui, A.; Mairal, J.; Chanussot, J. Image Processing and Machine Learning for Hyperspectral Unmixing: An Overview and the HySUPP Python Package. *IEEE Trans. Geosci. Remote Sens.* **2024**, *62*, 5517631. [CrossRef]
21. Hu, X.; Zhang, Z.; Zhai, J.; Zhang, L.; Tang, Y.; Peng, Y.; Zhou, T. EDTST: Efficient Dynamic Token Selection Transformer for Hyperspectral Image Classification. *Remote Sens.* **2025**, *17*, 3180. [CrossRef]

22. Dai, X.; Li, Z.; Li, L.; Xue, S.; Huang, X.; Yang, X. HyperTransXNet: Learning Both Global and Local Dynamics with a Dual Dynamic Token Mixer for Hyperspectral Image Classification. *Remote Sens.* **2025**, *17*, 2361. [CrossRef]
23. Li, Z.; An, W.; Guo, G.; Wang, L.; Wang, Y.; Lin, Z. SpecDETR: A transformer-based hyperspectral point object detection network. *ISPRS J. Photogramm. Remote Sens.* **2025**, *226*, 221–246. [CrossRef]
24. Van Wittenberghe, S.; Amin, E.; Pascual-Venteo, A.B.; Pérez-Suay, A.; Tenjo, C.; Sabater, N.; van der Tol, C.; Drusch, M.; Moreno, J. Retrieval of leaf-level fluorescence quantum efficiency and NPQ-related xanthophyll absorption through spectral unmixing strategies for future VIS-NIR imaging spectroscopy. *Remote Sens. Environ.* **2024**, *300*, 113879. [CrossRef]
25. Ochoa, F.; Brodrick, P.G.; Okin, G.S.; Ben-Dor, E.; Meyer, T.; Thompson, D.R.; Green, R.O. Soil and vegetation cover estimation for global imaging spectroscopy using spectral mixture analysis. *Remote Sens. Environ.* **2025**, *324*, 114746. [CrossRef]
26. Altmann, Y.; Dobigeon, N.; Tourneret, J.Y.; McLaughlin, S. Nonlinear hyperspectral unmixing using Gaussian processes. In Proceedings of the 2013 5th Workshop on Hyperspectral Image and Signal Processing: Evolution in Remote Sensing (WHISPERS), Gainesville, FL, USA, 26–28 June 2013; pp. 1–4. [CrossRef]
27. Halimi, A.; Altmann, Y.; Dobigeon, N.; Tourneret, J.Y. Nonlinear unmixing of hyperspectral images using a generalized bilinear model. In Proceedings of the 2011 IEEE Statistical Signal Processing Workshop (SSP), Nice, France, 28–30 June 2011; pp. 413–416. [CrossRef]
28. Tømmervik, H.; Julitta, T.; Nilsen, L.; Park, T.; Burkart, A.; Ostapowicz, K.; Karlsen, S.R.; Frans-Jan·Parmentier.; Pirk, N.; Bjerke, J.W. The northernmost hyperspectral FloX sensor dataset for monitoring of high-Arctic tundra vegetation phenology and Sun-Induced Fluorescence (SIF). *Data Brief* **2023**, *50*, 109581. [CrossRef]
29. Emde, C.; Buras-Schnell, R.; Kylling, A.; Mayer, B.; Gasteiger, J.; Hamann, U.; Kylling, J.; Richter, B.; Pause, C.; Dowling, T.; et al. The libRadtran software package for radiative transfer calculations (version 2.0.1). *Geosci. Model Dev.* **2016**, *9*, 1647–1672. [CrossRef]
30. Mayer, B.; Kylling, A. Technical note: The libRadtran software package for radiative transfer calculations—Description and examples of use. *Atmos. Chem. Phys.* **2005**, *5*, 1855–1877. [CrossRef]
31. Vicent, J.; Verrelst, J.; Sabater, N.; Alonso, L.; Rivera-Caicedo, J.P.; Martino, L.; Muñoz-Marí, J.; Moreno, J. Comparative analysis of atmospheric radiative transfer models using the Atmospheric Look-up table Generator (ALG) toolbox (version 2.0). *Geosci. Model Dev.* **2020**, *13*, 1945–1957. [CrossRef] [PubMed]
32. European Centre for Medium-Range Weather Forecasts. Copernicus Atmosphere Monitoring Service Data. European Union, Copernicus Programme. 2024. Available online: https://atmosphere.copernicus.eu/data (accessed on 15 December 2025).
33. Siegmann, B.; Quiros-Vargas, J.; Krämer, J.; Bendig, J.; Salattna, S.; Rascher, U. *Measuring Solar-Induced Chlorophyll Fluorescence (SIF) Across Scales: First Results from the LIAISE Field Campaign, July 2021;* LIAISE field campaign report/presentation; LIAISE: London, UK, 2021.
34. Morata, M.; Siegmann, B.; García-Soria, J.L.; Rivera-Caicedo, J.P.; Verrelst, J. On the potential of principal component analysis for the reconstruction of full-spectrum SIF emission and emulated airborne-to-satellite upscaling. *Remote Sens. Environ.* **2025**, *328*, 114865. [CrossRef]
35. Cogliati, S.; Celesti, M.; Cesana, I.; Miglietta, F.; Genesio, L.; Julitta, T.; Schuettemeyer, D.; Drusch, M.; Rascher, U.; Jurado, P.; et al. A Spectral Fitting Algorithm to Retrieve the Fluorescence Spectrum from Canopy Radiance. *Remote Sens.* **2019**, *11*, 1840. [CrossRef]
36. Lawson, C.L.; Hanson, R.J. *Solving Least Squares Problems*; Society for Industrial and Applied Mathematics: Philadelphia, PA, USA, 1995. [CrossRef]
37. Somers, B.; Cools, K.; Delalieux, S.; Stuckens, J.; Van der Zande, D.; Verstraeten, W.W.; Coppin, P. Nonlinear Hyperspectral Mixture Analysis for tree cover estimates in orchards. *Remote Sens. Environ.* **2009**, *113*, 1183–1193. [CrossRef]
38. Regaieg, O.; Malenovský, Z.; Siegmann, B.; Buffat, J.; Krämer, J.; Lauret, N.; Le Dantec, V. DART-based temporal and spatial retrievals of solar-induced chlorophyll fluorescence quantum efficiency from in-situ and airborne crop observations. *Remote Sens. Environ.* **2025**, *319*, 114636. [CrossRef]
39. Amoros-Lopez, J.; Gomez-Chova, L.; Vila-Frances, J.; Alonso, L.; Calpe, J.; Moreno, J.; del Valle-Tascon, S. Evaluation of remote sensing of vegetation fluorescence by the analysis of diurnal cycles. *Int. J. Remote Sens.* **2008**, *29*, 5423–5436. [CrossRef]
40. Hu, M.; Cheng, X.; Zhang, J.; Huang, H.; Zhou, Y.; Wang, X.; Pan, Q.; Guan, C. Temporal Variation in Tower-Based Solar-Induced Chlorophyll Fluorescence and Its Environmental Response in a Chinese Cork Oak Plantation. *Remote Sens.* **2023**, *15*, 3568. [CrossRef]
41. Bendig, J.; Malenovský, Z.; Siegmann, B.; Krämer, J.; Rascher, U. Comparing methods for solar-induced fluorescence efficiency estimation using radiative transfer modelling and airborne diurnal measurements of barley crops. *Remote Sens. Environ.* **2025**, *317*, 114521. [CrossRef]

42. Krämer, J.; Siegmann, B.; Kraska, T.; Muller, O.; Rascher, U. The potential of spatial aggregation to extract remotely sensed sun-induced fluorescence (SIF) of small-sized experimental plots for applications in crop phenotyping. *Int. J. Appl. Earth Obs. Geoinf.* **2021**, *104*, 102565. [CrossRef]
43. Campbell, P.K.E.; Huemmrich, K.F.; Middleton, E.M.; Ward, L.A.; Julitta, T.; Daughtry, C.S.T.; Burkart, A.; Russ, A.L.; Kustas, W.P. Diurnal and Seasonal Variations in Chlorophyll Fluorescence Associated with Photosynthesis at Leaf and Canopy Scales. *Remote Sens.* **2019**, *11*, 488. [CrossRef]